# Use of satellite derived cloud properties to quantify growing cumulus beneath cirrus clouds

John R. Mecikalski [a],*, Patrick Minnis [b], Rabindra Palikonda [c]

[a] Atmospheric Science Department, University of Alabama in Huntsville, NSSTC, 320 Sparkman Drive, Huntsville, AL 35805-1912, USA
[b] NASA Langley Research Center, Hampton, VA, USA
[c] Science Systems and Applications, Inc., Hampton, VA, USA

## ARTICLE INFO

## ABSTRACT

The accurate prediction of convective cloud development in advance of thunderstorm formation (so-called "convective initiation," CI) is a challenging forecast problem, one in which the processing of 5–15 min interval imagery from geostationary satellites (e.g., *Meteosat* Second Generation) offers considerable promise. A present drawback to using sequences of visible or infrared (IR) satellite images to monitor growing cumulus clouds is that higher altitude cirrus clouds often obscure the view of the low-level cumulus in the pre-convective environment. In particular, cirrus anvils from pre-existing convection, and cirrus caused by deep layer quasi-geostrophic ascent, are very common in pre-CI environments. Cloud derived parameters from GOES are used here to demonstrate how quantities like visible optical depth ($\tau$), emittance, liquid water path, and effective particle size can be used to quantify cumulus cloud growth in advance of CI. Time rates of change of these derived quantities, as well as IR interest fields that describe cumulus cloud development rates beneath cirrus, are analyzed as $\tau$ of the cirrus are binned from 1 to >50. Results confirm that if cirrus possess $\tau<20$, up to >90% of the "signal" in the IR interest field remains, compared to clear-sky values, and it is proposed that CI can still be adequately nowcasted using IR channel data similar to what is done in the absence of cirrus. Similarly, cloud derived parameters become valuable as their time rates of change measure cumulus cloud growth beneath the higher clouds. In contrast, once $\tau$ values increase beyond ~20, cumulus cloud growth signals decrease significantly through cirrus, and as $\tau$ becomes >40, little information from the cumulus remains.

© 2012 Elsevier B.V. All rights reserved.

## 1. Introduction and motivation

Ongoing research is focused on the detection of so-called "convective initiation" (CI) of new convective storms using time sequences of geostationary satellite observations of growing cumulus clouds, which provide valuable and unique information in advance of radar observed precipitation. For this study, CI is defined as the first occurrence of a $\geq 35$ dBZ radar echo at the $-10$ °C altitude, as well established by previous studies (Browning and Atlas, 1965; Marshall and Radhakant, 1978; Schreiber, 1986; Wilson and Schriber, 1986; Wilson et al., 1992; Wilson and Mueller, 1993; Mueller et al., 2003; Roberts and Rutledge, 2003).

The geostationary satellite observations are in the visible (VIS) and infrared (IR) spectrum (0.365–13.4 microns, μm) and available every 5–15 min from instruments including the Geostationary Operational Environmental Satellite (GOES), *Meteosat* Second Generation (MSG) Spinning Enhanced Visible Infra-Red Imager (SEVIRI), as well as the Chinese Fengyun (e.g., FY–2 F), and the Japanese Multi-Functional Transport Satellite (MTSAT-2). The main limitations in CI nowcasting algorithms presently are related to the following: (1) sensor resolution in the IR channels being mostly above the cumulus cloud scale (3–4 km in IR), (2) the ability to accurately and consistently detect cumulus clouds in satellite imagery, and (3) difficulties in tracking early-growth cumulus clouds across successive images while focusing on the realistic scales of the main updraft, which is related to sensor resolutions being too low. More optimal IR

* Corresponding author.
*E-mail address:* john.mecikalski@nsstc.uah.edu (J.R. Mecikalski).

field resolutions for thunderstorm nowcasting using satellite data are 0.375 to 2 km, which are presently (publicly) available only on polar orbiting sensors that have overpass repeat cycles far too low to capture the rapid evolution of growing cumulus clouds [e.g., the MODerate Resolution Imaging Spectroradiometer (MODIS; repeat cycle of up to ~4 h in Midlatitudes (when both the *Terra* and *Aqua* instruments are considered, and/or from the Visible Infrared Imaging Radiometer Suite (VIIRS) instrument].

One of the more robust approaches in 0–1 h CI nowcasting is the SATellite Convection AnalySis and Tracking (SATCAST) system that processes a sequence of 2–3 day and night images spaced 5–15 min apart per nowcast, using the cloud classification algorithm of Berendes et al. (2008) and cloud object tracking method of Walker et al. (in press; see Mecikalski and Bedka (2006). The SATCAST methodology is based on the early detection of new storm development offered by satellite (as satellite VIS and IR data "see" clouds), whereas operational S- and C-band radar cannot detect clouds, requiring instead the presence of significant hydrometeors with sizes larger than a few millimeters. Sieglaff et al. (2011) present a method of cumulus cloud growth monitoring, that combines the 10.7 μm IR channel cooling rate thresholds of Roberts and Rutledge (2003) and a "box averaging" tracking approach. Procedures as employed in SATCAST, specifically threshold-based scoring using multiple IR channels, channel differences, and time trends of single and multiple channel differences (Mecikalski et al., 2010), are being applied in current and forthcoming upgrades to convective storm nowcasting systems, like those developed by the Nowcasting Satellite Analysis Facility (SAF) as supported by the European Organisation for the Exploitation of Meteorological Satellites (EUMETSAT), and the Corridor Integrated Weather System (CIWS) as supported by the Federal Aviation Administration (Iskenderian et al., 2009).

It is generally agreed that ground and space based C-, S- and Ku/Ka band radar platforms are limited, not being able to adequately nowcast the CI process because they cannot adequately observe kinematic processes in early stage (0–30 min) cumulus clouds, and/or are unable to observe precipitating hydrometeors (smaller than ~10 μm in diameter) until CI has actually occurred. Therefore, geostationary satellites play a vital role in the thunderstorm forecast problem because developing cumulus clouds are readily observed in VIS and IR data 15–60 min in advance of precipitation formation. However, when cumulus cloud development is obscured by middle or higher level clouds, satellite-based methods have been known to fail simply because the cumulus clouds are not identified (in lieu of the higher clouds), or cannot be identified due to the obscuration, and therefore cannot be tracked and monitored (related to points 2 and 3 above).

As thunderstorm nowcasting is a significant problem in operational weather forecasting, especially related to aviation applications (Murray, 2002; Mecikalski et al., 2007), the motivation is high to capture as many occurrences of CI in satellite observations as possible, whereas nowcasting CI correctly is a matter involving proper use of VIS and IR datasets toward linearly extrapolating cloud growth trends. The obscuration of cumulus clouds by higher level altocumulus, altostratus or cirrus-type clouds typically results in most cloud typing algorithms classifying the dominant cloud type as the observable cloud, or defining a "multi-layer" cloud scene. Yet, in many cases, experts trained in satellite analysis can see growing cumulus clouds in the presence of other clouds, especially when the overlying cirrus clouds are "thin" (Min and Duan, 2005), or not too thick that VIS light cannot penetrate upward from beneath, enough to discern the lower level cumuli. As examples, Fig. 1(a–f) shows cases of growing cumulus occurring beneath veils of cirrus clouds over 30 min periods in 1 km resolution GOES VIS channel data, in which the cirrus clouds at an initial time ($t$) gradually increase in terms of visible optical depth ($\tau$), from Fig. 1a to f. In Fig. 1, the top row (a) represents growing cumulus clouds at time $t$ (far left) in which the estimated $\tau$ of the "cirrus–cumulus cloud system" is between 1 and 10, whereas by time $t + 30$ min (far right), $\tau$ values have increased to those typically found in deep convective clouds, near or greater than 40 (Hong et al., 2007). Fig. 1(b–f), demonstrates increasing initial time-$t$ and $\tau$ values, and hence an increasing difficulty in visually detecting and quantifying the growth of the underlying cumulus clouds.

In many ways, this study follows on that of Mecikalski et al. (2011) in which it was determined how to interpret cloud-derived parameters for growing cumulus clouds in advance of CI, specifically cloud $\tau$, cloud-top pressure, and particle effective radius. Mecikalski et al. (2011) found that cumulus cloud growth is quantifiable in $\tau$ fields regardless of the sky condition, specifically the pre-CI sky conditions do not need to be completely clear above the developing cumulus clouds in order for cloud growth to be detected. Therefore, this study addresses several specific questions: (1) How thin (in terms of $\tau$) does cirrus need to be before they completely obscure the underlying lower/cumulus clouds, such that signals of growing cumulus clouds in IR and cloud parameter data can no longer be quantified? Subsequently, (2) what value of $\tau$ is associated with cirrus that are too thick for growing cumulus to be detectable and quantified beneath? (3) When the cirrus are thin, how and what IR and derived cloud parameter fields can be used to evaluate growing cumulus clouds? And, (4) when overlying clouds are present, can derived cloud parameters be used to characterize growing convective clouds better than simple IR channel data?

We refer again to Fig. 1 as it introduces the methodology of this study, whereas the $\tau$ and other data used herein will be discussed in Section 2. In Fig. 1, the rows (a–f) show examples of cumulus cloud development occurring beneath cirrus clouds of increasing $\tau$ at time $t$, from (a) 1–10 to (f) > 50. As seen, once the $\tau$ increases to > 13 (Fig. 1b) the cumuli are significantly visually obscured from view, and the main turrets or updrafts become visible by $t + 30$ min only when they protrude through the cirrus cloud shield. The processing methodology is described in Section 3, and the main results will be discussed in Section 4. Section 5 concludes the paper.

## 2. Data and quality estimates

The datasets used in the analysis are as follows: (1) GOES 1 km VIS 0.651 μm and IR 3.9, 6.5, 10.7 and 13.3 μm channel data, (2) derived cloud parameters, that rely upon GOES VIS and IR data, and (3) National Weather Service Weather Surveillance Doppler Radar (WSR-88D) base-level reflectivity observations within the National Mosaic and Multisensor QPE (NMQ) dataset. The GOES 1 km VIS data were used for case identification, whereas 253 events were

## a) 31 May 2011
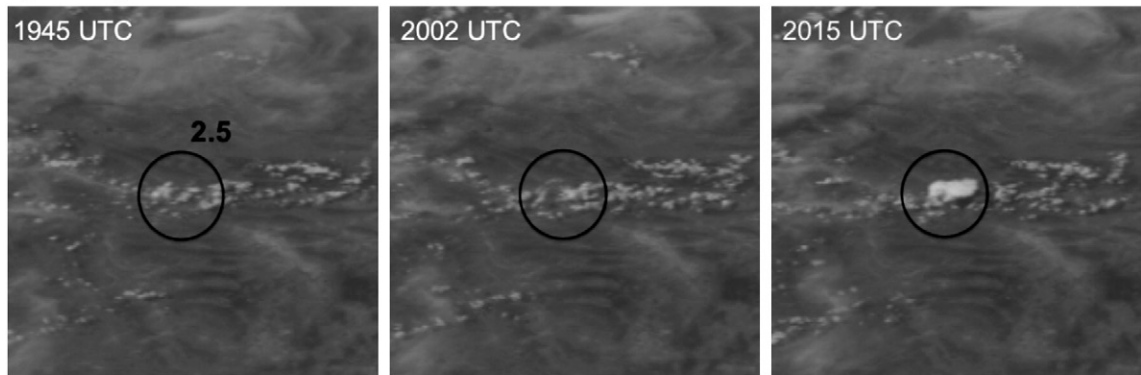


## b) 26 April 2011
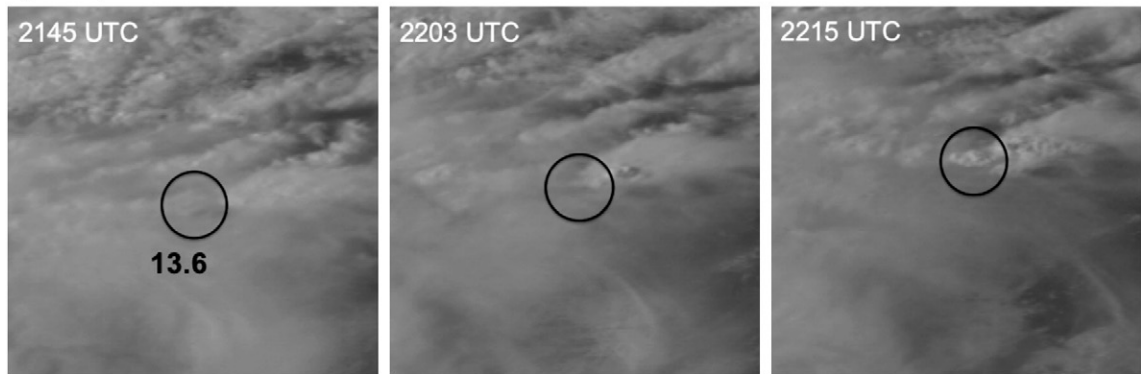


## c) 29 May 2011
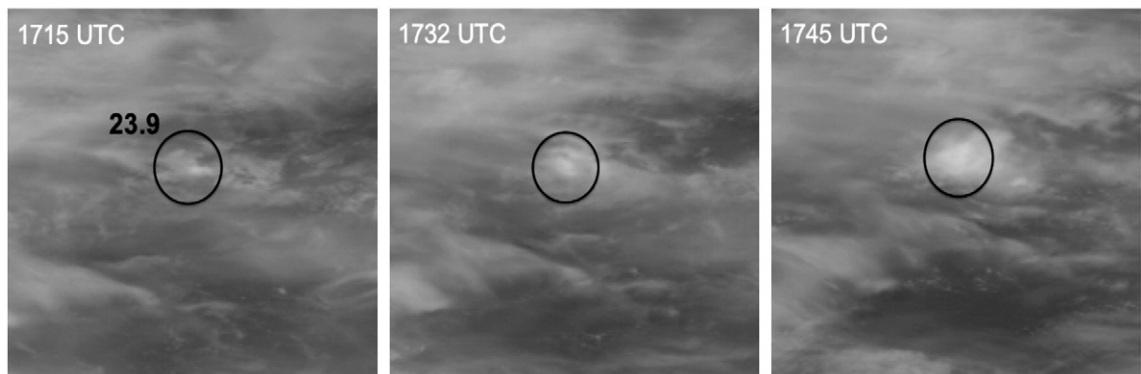


**Fig. 1.** Cases of CI occurring beneath cirrus (and other higher) cloud types as seen in GOES-13 imagery. The top row (a) represents growing cumulus clouds a time $t$ in which the estimated visible optical depth ($\tau$) values are between 1 and 10, whereas by time $t + 30$ min, $\tau$ values have increased to those typically found in deep convective clouds, near 40 (Hong et al., 2007). Other examples (b–f) demonstrate increasing initial time ($t$) $\tau$ values and an increasing difficulty in visually seeing the presence and growth of the underlying cumulus clouds. Results in Tables 1 and 2 are categorized into $\tau$ bins as shown in panels a–f.

initially identified in the months April–May 2011, for cumulus clouds developing beneath cirrus clouds over a region covered by the GOES-13 satellite, specifically between 66.2° and 104.5° W, and 16.0° and 45.6° N. Data from 1415 through 2345 UTC were used to capture daytime CI events when VIS channel data can be used, and when the presence of cirrus clouds prior to rapid cumulus cloud development can be confirmed. Due to missing cloud parameter data for several hours, 248 events were used in the analysis to follow. All cases were documented by a human expert, with the goal being to capture clouds from an early *cumulus mediocris* and "towering cumulus" stage to the later-time *cumulonimbus* (or near *cumulonimbus*) stage of development, as done in Mecikalski et al. (2010). Given the time frequency of the cloud properties data (see below), all 248 events were cataloged over 30–min time periods, and care was taken to collect events in which cumulus clouds were far from the precipitation stage at time $t$ at 15 or 45 min after the top of an hour, and then near or at the *cumulonimbus* stage 30 min

**d) 29 May 2011**

2145 UTC · 31.7 | 2202 UTC | 2215 UTC

**e) 30 May 2011**

2215 UTC · 45.9 | 2233 UTC | 2245 UTC

**f) 29 May 2011**

1815 UTC · 65.7 | 1832 UTC | 1845 UTC
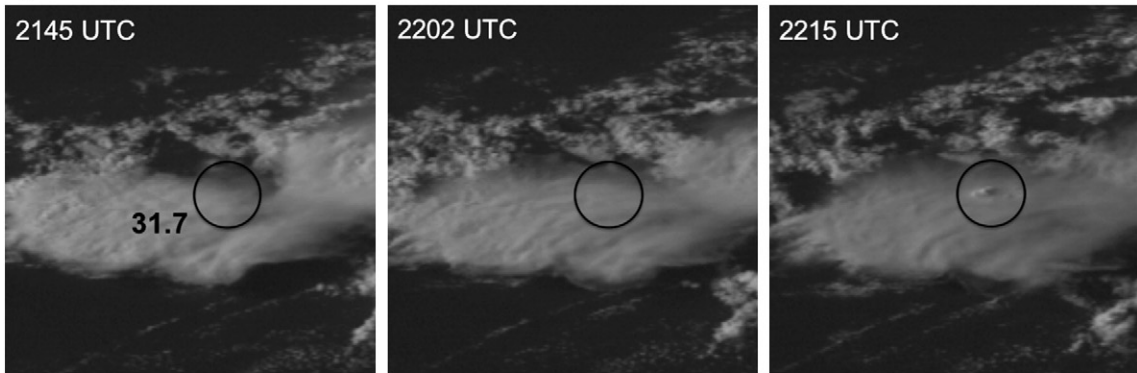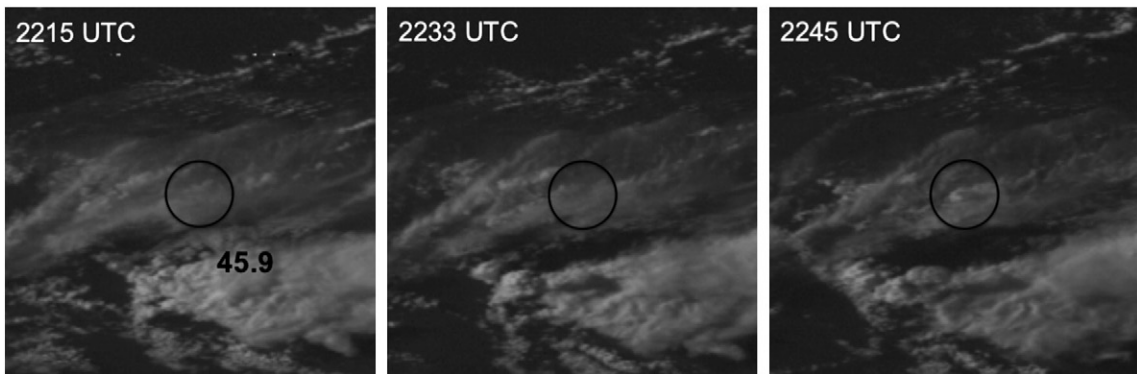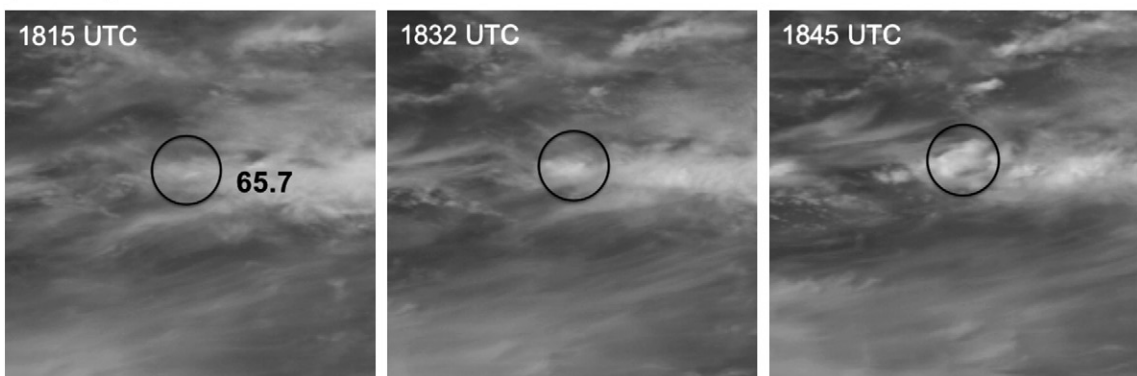
**Fig. 1** (*continued*).

later (time $t + 30$ min). Thus, all cases then occurred between 15 and 45 min within a clock hour, or between 45 min after an hour to 15 min past the top of the following hour (e.g., between 1615 and 1645 UTC, or between 2045 and 2115 UTC, respectively).

The NMQ reflectivity fields (Zhang et al., 2011) were obtained from the National Severe Storms Laboratory (NSSL), a seamless high-resolution national radar mosaic developed from ~140 WSR-88D radars in the continental United States and 31 C-band weather radars in southern Canada. The comparison to radar imagery was done to prove that CI did occur for all cases at or after the $t + 30$ min time. A quantitative comparison to rainfall intensity (in terms of future-time dBZ values) was instead not

done, as the main motivation for this study is the characterization of *growing cumulus clouds* in advance of CI. Therefore, the results of the study apply strongly to nowcasting CI.

From the GOES-13 cloud parameter dataset (discussed below), derived 0.651 μm VIS reflectance ($\rho$; fractional percentage), 10.7 μm cloud top brightness temperature ($T_B$; K), emittance ($\varepsilon$; unitless), $\tau$ (unitless), particle size ($r_e$; μm), cloud water path [CWP; mg(cm)$^{-2}$], cloud top height ($C_z$; km), cloud effective height ($C_e$; km), and cloud base height ($C_b$; km) were used. For "optically thick" clouds ($\tau > 6$), $C_e$ is equivalent to $C_z$ as determined using the atmosphere-corrected 10.7 μm $T_B$; for "optically thin" clouds ($\tau \leq 6$), $C_e$ lies between $C_b$ and $C_z$ as

**Table 1**

Binned vertical optical depth ($\tau$), averaged over events, of 0.651 μm VIS reflectance ($\rho$; fractional percentage), 10.7 μm cloud top brightness temperature ($T_B$; K), emittance ($\varepsilon$; unitless), $\tau$ (unitless), liquid water path [CWP; mg(cm$^2$)], particle size ($r_e$; μm), cloud top height ($C_z$), cloud effective height ($C_e$), and cloud base height ($C_b$). Also shown are 30-min changes in $\rho$, $\varepsilon$, $\tau$, CWP, $C_z$ and $T_{B30}$, denoted by the "30" subscripts. See text for discussion of the behavior of these quantities.

| Initial $\tau$ | 01–10 | 11–20 | 21–30 | 31–40 | 41–50 | >50 |
|---|---|---|---|---|---|---|
| Events | 89 | 63 | 37 | 15 | 11 | 33 |
| $\rho$ | 0.38 | 0.62 | 0.73 | 0.77 | 0.79 | 0.89 |
| $T_B$ | 261.6 | 244.3 | 232.8 | 236.7 | 239.0 | 232.1 |
| $\varepsilon$ | 0.011 | 1.001 | 1.002 | 0.993 | 1.001 | 1.003 |
| CWP | 0.07 | 0.23 | 0.53 | 0.72 | 0.78 | 1.75 |
| $\tau$ | 5.0 | 14.2 | 24.3 | 33.5 | 44.0 | 89.7 |
| $r_e$ | 19.5 | 26.9 | 34.7 | 28.6 | 29.9 | 30.8 |
| $C_z$ | 6.7 | 9.9 | 11.5 | 11.2 | 11.0 | 11.1 |
| $C_e$ | 5.9 | 8.5 | 10.1 | 9.7 | 9.6 | 9.8 |
| $C_b$ | 4.7 | 5.1 | 5.7 | 5.2 | 4.7 | 4.3 |
| $\rho_{30}$ | 0.30 | 0.19 | 0.11 | 0.04 | 0.15 | −0.02 |
| $\varepsilon_{30}$ | 0.508 | −0.024 | −0.004 | 0.008 | 0.000 | −0.002 |
| $\tau_{30}$ | 34.9 | 47.8 | 52.8 | 29.4 | 55.4 | 0.4 |
| CWP$_{30}$ | 0.69 | 1.02 | 1.23 | 0.58 | 1.24 | 0.17 |
| $C_{z30}$ | 3.1 | 1.1 | 0.7 | 0.5 | 1.2 | 1.1 |
| $T_{B30}$ | −19.6 | −12.1 | −4.9 | −3.2 | −10.4 | −7.7 |

**Table 2**

Interest fields for convective and first-flash lightning initiation, binned according to visible optical depth ($\tau$). See text for discussion of the behavior of these quantities. Values for $\rho$ and $\rho_{30}$ are in fractional percentage. Values of all channel difference and 30-min time rate of change fields are in °C, while $T_B$ data are in degrees Kelvin. In the last two columns, "MB06_CI" refers to "Mecikalski and Bedka (2006) CI interest fields threshold values," and "Harris_LI" refers to "Harris et al. (2010) LI interest field threshold values.

| Initial $\tau$ | 01–10 | 11–20 | 21–30 | MB06_CI | Harris_LI |
|---|---|---|---|---|---|
| Events | 89 | 63 | 37 | | |
| $\rho$ | 0.38 | 0.62 | 0.73 | n/a | <0.11 |
| 30-min $\rho$ trend | 0.30 | 0.19 | 0.11 | n/a | ≤ −0.04[b] |
| $T_B$ | 261.6 | 244.3 | 232.8 | <273 | <273 |
| 30-min $T_B$ trend | −19.6 | −12.1 | −4.9 | <−4 | ≤ −12[b] |
| $T_{3.9-10.7\ \mu m}$ | 20.1 | 22.0 | 24.2 | n/a | <17 |
| $T_{6.5-10.7\ \mu m}$ | −25.9 | −12.9 | −6.5 | −35 to −10 | ≥ −30 |
| $T_{13.3-10.7\ \mu m}$ | −14.8 | −7.7 | −4.3 | −25 to −10 | ≥ −13 |
| 30-min $T_{3.9-10.7\ \mu m}$ trend | 4.9 | 2.7 | 2.7 | n/a | >3[b] |
| 30-min $T_{6.5-10.7\ \mu m}$ trend | 12.5 | 4.7 | 1.7 | >6[a] | >10[b] |
| 30-min $T_{13.3-10.7\ \mu m}$ trend | 7.3 | 2.4 | 1.1 | >6[a] | >8[b] |

[a] Values are doubled from per 15 min rates, as shown in Mecikalski and Bedka (2006).
[b] Values are doubled from per 15 min rates, as shown in Harris et al. (2010).

dictated by $\varepsilon$ or cloud transparency (Smith et al., 2008). For ice clouds, the retrieved field of effective diameter ($d_e$) is divided by 2, and all values presented here are then $r_e$. For CWP, as the "cirrus–cumulus cloud system" is analyzed, this quantity pertains to combined liquid and ice water paths, to make a total CWP. Given 30 min over which each event was observed, 30-min time trends in several fields were determined, those being $\rho$ ($\rho_{30}$), $T_B$ ($T_{B30}$), $\varepsilon$ ($\varepsilon_{30}$), $\tau$ ($\tau_{30}$), CWP (CWP$_{30}$), and $C_z$ ($C_{z30}$). These time trends will be valuable toward answering some of the above questions, as well as in estimating how these data can be eventually used in applications that monitor thunderstorm development.

The GOES-13 cloud parameter data are from the National Aeronautics and Space Administration (NASA) Langley Research Center, Cloud and Radiation Group near-real time products (http://www-angler.larc.nasa.gov). Though nominally having a 4-km resolution, the analyzed radiance data are sampled at $8 \times 8$ km horizontal resolution every 30 min, 15 and 45 min past the top of each hour. The daytime cloud parameters were derived using the visible infrared shortwave-infrared split window technique (VISST; Minnis et al., 2008, 2011a) developed for the Clouds and Earth's Radiant Energy System (CERES) project (Wielicki et al., 1998). The GOES-13 VIS channel was calibrated against the MODerate resolution Imaging Spectroradiometer (MODIS) 0.63-$\mu m$ channel following the procedures of Minnis et al. (2002). Validation of the VISST-derived parameters has been performed using surface, aircraft, and other satellite borne sensors (Minnis et al., 2011b and references therein; Zheng et al., 2011; Painemal et al., submitted for publication). The comparisons were mostly conducted for single-layer overcast stratus or cirrus cloud cases owing to the challenges involved for multilayer and cumulus cloud validation. Even for "uniform" overcast clouds, errors in matching sensor fields of view and in the reference instrument retrievals themselves introduce significant errors into the validation. It is even more difficult using surface-based or aircraft sensors to determine the properties definitively in broken clouds or overlapping clouds than for the simpler cloud morphologies. With respect to cumulus clouds specifically, observational obstacles make the VISST cloud parameter validation more challenging. These include, among others, rapid cloud evolution, difficulty in obtaining in-cloud measurements when updraft strengths are large (>20 ms$^{-1}$, making aircraft flights dangerous), and very high cloud-to-cloud variability (leading to quality estimates over cumulus fields being highly variable and often unrepresentative).

For this study, we focus mostly on cloud properties for optically thin ($\tau<6$) cirrus over optically thick ($\tau>6$) cumulus clouds. Although the presence of cirrus over liquid clouds will bias the satellite-retrieved $\tau$'s and CWPs (Minnis et al., 2007), the focus of this analysis is on relative changes in cloud properties over time, and therefore the use of 30-min time changes in the fields effectively removes systematic and bias-type errors. Given

**Fig. 2.** Similar to Fig. 1 (also GOES-13 images), as examples of CI occurring beneath cirrus with initial-time $\tau$ values <15 on 31 May 2011, increasing from top (a) to bottom (d) as labeled on image. These are shown to exemplify the highly varying scenes in which CI and LI may be nowcasted, and in particular, when the cumulus beneath the cirrus may not be seen in visible imagery.

a) 31 May 2011
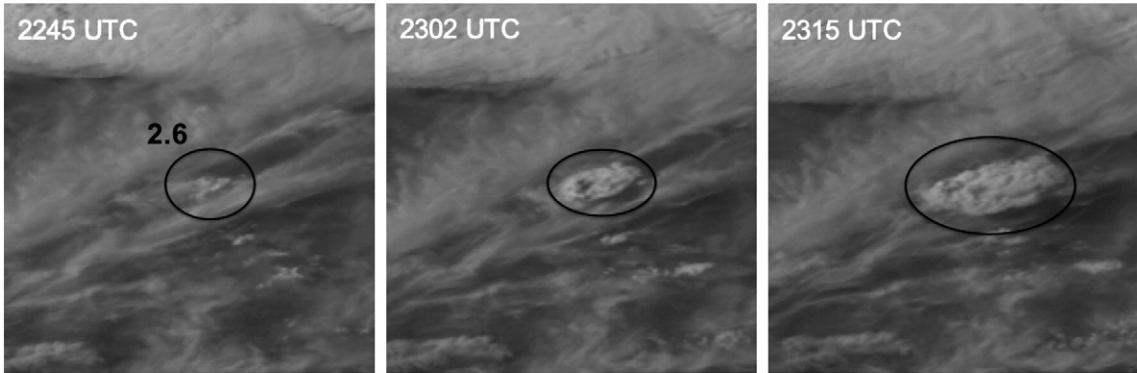


b) 31 May 2011
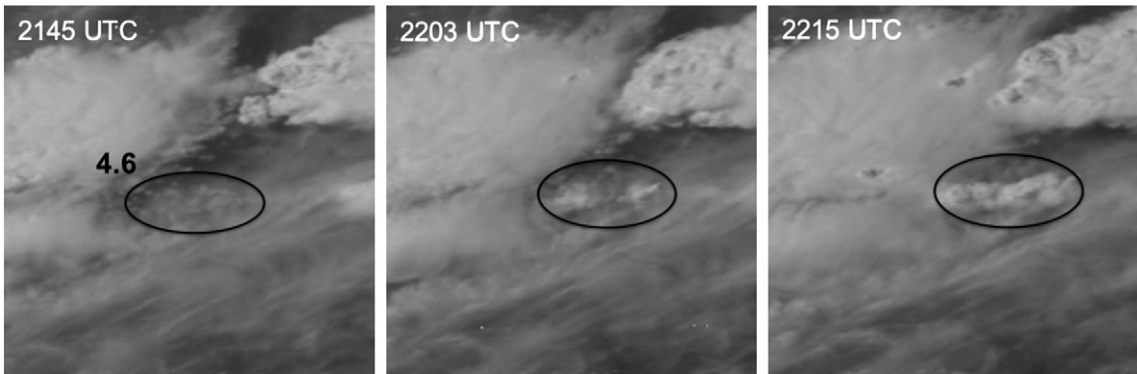


c) 31 May 2011
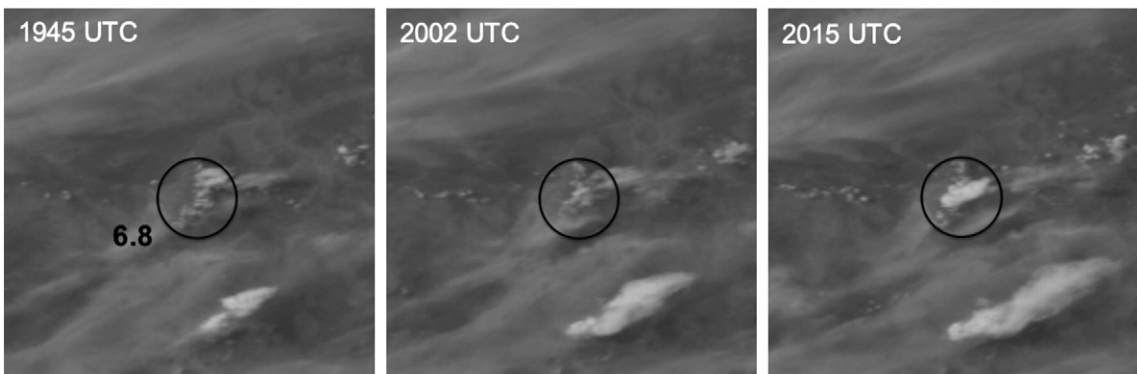


d) 31 May 2011
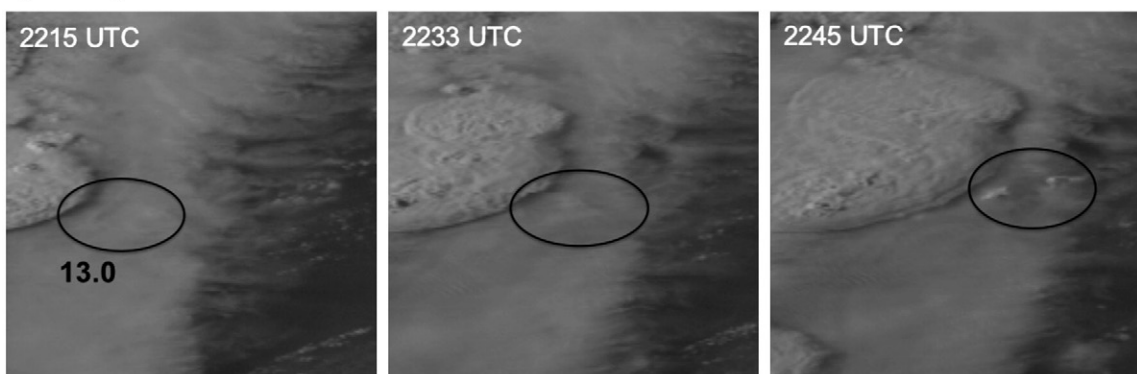
the comparisons between GOES-VISST retrieved fields and those obtained from other satellite sensor data (e.g., MODIS Aqua and Terra) we feel confident, after taking into account data/time matching and reference sensor uncertainties, that the instantaneous $\tau$ results are within 20% of some truth value, albeit obtaining "truth" is an equally challenging problem when comparing satellite derived quantities to aircraft or retrievals from surface-based instruments, as noted above [see also Min and Harrison (1996) and Trishchenko et al., 2001]. As discussed in the following section, the results for the 248 events are averaged into six $\tau$ bins, which further reduces the "noise" in these retrievals caused by mismatches between the individual clouds being sampled at 4-km resolution in GOES, and the 8-km resolution VISST data.

## 3. Processing methodology

Given that the main focus of this study is to evaluate the objective detection of growing cumulus beneath cirrus clouds using satellite fields, $\tau$ is a baseline dataset for categorizing events and organizing the interpretation of the VISST and IR channel fields, for addressing the questions posed above. Bins with $\tau$ values >40 represent examples where cumulus cloud development should be largely obscured thick cirrus and/or middle level clouds (Hong et al., 2007), while bins with $\tau < 30$ represent events where at least some information on the underlying clouds resides in the VISST and IR datasets. As shown above, Fig. 1(a–f) exemplifies cases in $\tau$ bins (a) 1–10, (b) 11–20, (c) 21–30, (d) 31–40, (e) 41–50, and (f) ≥51. The latter two bins [Fig. 1(e–f)] show main convective updrafts poking through the higher clouds around $t+16$ to $t+30$ min, in which it is challenging to determine whether any cloud parameters may have identified cumulus cloud growth in these situations. The maximum value of $\tau$ in these data is 128, with missing or clear sky values set to −9.

Once the $\tau$ bins were formed, the VISST cloud parameters were also binned, and the 30 min time trends were computed. Next, the CI and lightning initiation (LI) interest fields as developed in Roberts and Rutledge (2003), Mecikalski and Bedka (2006) and Harris et al. (2010) are also computed to determine under what conditions they may still show useful information, in "thin" cirrus situations. Although this study does not focus on LI nowcasting, the similarity in the CI and LI interest fields (in terms of IR channels used, and spectral information considered) is such that evaluating both of these together in this study makes sense, considering both CI and LI components are within the SATCAST system, and because both nowcast types are heavily influenced by the presence of cirrus obscuring initial cumulus cloud development.

## 4. Results

Table 1 presents the categorical $\tau$ results, within the $\tau$ ranges 1–10, 11–20, 21–30, 31–40, 41–50, and ≥51 [as in Fig. 1(a–f)]. All events in which $\tau$ values were >50 at time $t$ were grouped, to the maximum value of 128.

From Table 1, static bin-to-bin values of $\rho$, $T_B$, $\varepsilon$, CWP, $\tau$, $r_e$, $C_z$, $C_e$ and $C_b$ are seen to change most rapidly until $\tau$ is ≥20. In other words, as $\tau$ increases between 0 and 30, sub-cirrus cloud information becomes attenuated quickly. In particular, $\rho$ increases from 0.383 to 0.726, after which it increases more slowly

(0.726 to 0.889, between $\tau = 21$ to $\tau \geq 51$). With $\tau \leq 10$, $T_B$ values show influences from both ground and cloud-top temperatures within the $8 \times 8$ km pixels, as $T_B$ averages are near 262 K; then, the $T_B$'s become more indicative of cirrus cloud tops as $\tau$'s exceed 20, decreasing to ≤239 K. CWP values increase by 3, 6 and 10 times [0.07 to 0.53 mg (cm)$^{-2}$] as $\tau$ values increase from 20 to 30 and toward 40, respectively, which is consistent with the VISST methodology as higher $\tau$ will be correlated to increasing CWP (Smith et al., 2008; Minnis et al., 2011a; see also Watts et al., 1998). Importantly, average $\tau$ values within each bin are near the midpoint, showing a uniform distribution across the 248 event dataset on a per $\tau$-category basis.

Values of $r_e$ increase as $\tau$ increases to 30. The dual contributions from both developing cumulus and cirrus cloud types lead to a steady increase in average $r_e$ to near 35 μm. As the cirrus clouds fill the scene, $r_e$ values decrease some to <30 μm, possibly indicative of the formation of more uniform size distributions in the cirrus and particle settling (Haag and Kärcher, 2004; Westbrook et al., 2007). Cloud top values for optically thick ($C_z$) and optically thin ($C_e$) clouds show a consistent increase with time until $\tau$ exceeds ~20. $C_e$ values are less easily interpreted as these results include contributions from clouds at both layers (Smith et al., 2008). $C_b$ values are steady near 5 km, verifying deepening clouds in the scene when considered with $C_z$.

The time rate of change fields $\rho_{30}$, $\epsilon_{30}$, $\tau_{30}$, CWP$_{30}$, $C_{z30}$, and $T_{B30}$ are also shown in Table 1. These are developed to help answer the questions above. Values of $\rho_{30}$ are >0.30 in the first $\tau$ category, and then rapidly fall to <0.10 as a rule. Similarly, the largest values of $\epsilon_{30}$ occur when the cirrus clouds have $\tau < 10$, with steady values independent of $\tau$ as it increases to >10; $\epsilon_{30}$ values become small and fluctuate somewhat randomly between ± 0.01 especially as $\tau$ increases beyond 21. Therefore, both $\rho_{30}$ and $\epsilon_{30}$ become insensitive at higher $\tau$. $\tau_{30}$ and CWP$_{30}$ show sensitivity (larger change magnitudes with increasing $\tau$) in the first three categories, until $\tau$ values exceed 30. There are indications that larger changes in $\tau$ and CWP occur until $\tau$ reaches 50, which suggests that these two fields would have more value than other parameters diagnosing cumulus cloud growth even when cirrus are very thick (i.e. time rates of changes could be monitored in regions of known cirrus cloud canopies, with $\tau \leq 50$). Values of $C_{z30}$ show positive altitude changes, i.e. cumulus cloud growth, until $\tau$ become >20, with more random behavior thereafter.

For the last 30-min time-change field in Table 1, $T_{B30}$, interesting patterns are seen. First, within the 89 event 1–10 $\tau$ bin, the averaged $T_{B30}$ value is − 19.6 °C, which is much greater in magnitude than that found by Roberts and Rutledge (2003) for convective clouds in advance of CI [i.e. ≤ − 8 °C(30 min$^{-1}$)]. Second, for the 11–20 $\tau$ bin, the − 12.1 K $T_{B30}$ value shows contributions from the colder, higher level cirrus clouds within an 8 km$^2$ pixel, but is also well below the "clear-sky" Roberts and Rutledge threshold range. Given the behavior of the $T_{B30}$ field, Table 2 presents 10 interest fields as developed and demonstrated in Mecikalski and Bedka (2006) and Harris et al. (2010), which can specifically guide users of geostationary satellite observations on when these data will and will not provide value when 0–1 h nowcasting CI and first-flash LI beneath cirrus, respectively. As above, the events in Table 2 are subset by $\tau$ values ≤10 (89), between 11 and 20 (63), and between 21 and 30 (37); the original threshold values for CI and LI are also

shown. In place of the 3.9 μm $\rho$ as shown in Harris et al. (2010), the VISST $\rho$ values are shown, and therefore only a qualitative comparison between $\rho$ fields can be made.

Similar to $T_B$ and $T_{B30}$, with $\tau \leq 10$, values of channel difference fields 3.9–10.7 μm, 6.5–10.7 μm, 13.3–10.7 μm, and the 30-min 3.9–10.7 $\mu$m, 30-min 6.5–10.7 μm and 30-min 13.3–10.7 μm time trends, are all within the threshold ranges defined in Mecikalski and Bedka (2006) and Harris et al. (2010; see also Ackerman, 1996; Schmetz et al., 1997; Ellrod, 2004) for clear-sky growing cumulus cloud conditions. Average $\rho$ and $\rho_{30}$ values are however not consistent with those found in Harris et al. (2010), as $\rho$'s are much larger than 0.11 and 30-min changes in $\rho$ are positive. These behaviors in $\rho$ may be due to the brighter cumulus clouds within the scene, and contributions from clouds containing liquid hydrometeors versus ice. Within the second $\tau$ bin, except for $\rho$ and $\rho_{30}$, field values remain within the defined clear-sky critical threshold ranges, yet are all smaller in magnitude. As $\tau$ values reach and exceed 30, the IR contributions from cirrus overwhelm those from the cumulus clouds, except for the $T_B$ and $T_{B30}$ fields.

Implications from Table 2 results are that cirrus, middle level and/or multi-level cloud scenes in GOES observations with cloud system $\tau < 20$ are "thin enough" for an objective algorithm to be able to discern growing convective clouds beneath, and to provide nowcasts of CI and LI with some level of confidence (much as can be done in clear sky conditions). As examples of growing cumulus clouds in advance of CI, occurring with $\tau < 15$ and where data in Tables 1 and 2 will operate reasonably well for diagnosing cumulus growth, Fig. 2(a–d) shows 30-min sequences of growing cumulus clouds in GOES 1 km VIS satellite imagery. In Fig. 2(a–d), the $\tau$ value at time $t$ for the 8 km pixel is shown, and these represent cases similar to Fig. 1a. This is done to demonstrate how visually different low (<15) $\tau$ scenes can appear in VIS imagery; the ability to see VIS light (i.e. $\rho$) from bright cumulus clouds beneath a thin veil of cirrus, in essence, clouds that are composed of water drops versus ice crystals, is a function of sun angle, whereas high sun angles and mid-day images (1945–2015, Figs. 1a and 2c) make beneath-cirrus cloud observations somewhat easier. In contrast, Fig. 2d shows a later afternoon (2215–2245 UTC) case when cirrus clouds with $\tau < 15$ (13.0 in this case) completely mask developing cumulus clouds beneath.

It is important to note that 30-min observation frequencies are nearly too low for use in a real time or operational system that nowcasts CI and LI. There are several reasons for this, including: (1) cumulus clouds often deepen explosively within timeframes $\leq 15$ min, making 30-min data too infrequent to capture the main growth signal; and, (2) when tracking clouds or cloud objects, tracking errors can be large when using 30-min data from a geostationary sensor, based on the increased likelihood of missed objects due to incorrect velocity determinations, cumulus clouds evolving too rapidly, or due to nonlinear cloud motions in high vertical wind shears within severe storm environments, as noted in Mecikalski et al. (2008) and Walker et al. (in press). However, the use of 8 km resolution fields in this study helps minimize tracking errors, albeit all tracking was done by a human expert. The goal when using GOES VISST (or similar) cloud parameters within a thunderstorm nowcasting system should be to produce them as near to the native temporal and spatial resolutions of the geostationary platform as possible (e.g., 3 km

sampling distance, every 5 min for MSG), which is the goal within the NASA Langley Research Center.

## 5. Conclusions

Given the need to accurately nowcast thunderstorm formation (i.e. CI and LI) over 0–1 h timeframes, one must exploit 5–15 min geostationary satellite observations as a means to identify and monitor cumulus cloud growth, well in advance of presence of radar-detected precipitation. This study advances our understanding by quantifying how cloud derived (or satellite retrieved) parameters using the VISST algorithm for GOES can be used for such monitoring, when sky conditions in the pre-convective environment are not completely cloud free, and middle and especially higher altitude cirrus clouds are present. As many pre-convective storm environments are highly dynamical (in the presence of strong quasi-geostrophic forcing), and that anvil cirrus from nearby storms are often present in the vicinity of new storms developing in the late afternoon and evening, application of these results should allow satellite-based CI and LI nowcasts to be made in what were previously thought to be less than ideal situations, i.e. cases when the cumulus clouds are slightly to totally hidden from view.

For this study, we posed four main questions. The main conclusions are the following, which come from the interpretation of the results in Tables 1 and 2.

1. Values of $\tau > 20$ are found when the cumulus cloud growth signals in IR and VISST fields are nearly obscured, mostly making $\tau$ bin-to-bin and 30 min changes in cloud parameters fields, and hence the CI and LI interest fields, invariant or more randomly varying as $\tau$ increases.
2. When scene $\tau$ values are $\leq 20$, cirrus clouds are "thin enough" that useful quantification of cumulus cloud growth can be made. This conclusion is reached as the main signal magnitudes in the IR channels, channel differences, and time rate of change in CI and LI interest fields are >90% of those found in studies that focus on cumulus cloud development in clear-sky conditions. This is especially the case when $\tau$ is less than ~10. Similarly, robust and consistent (as a function of increasing $\tau$) average 30-min time changes in cloud parameters are found to be strongly related to cumulus cloud development with $\tau \leq 20$.
3. When scene $\tau$ values are $\leq 20$, bin-averaged $\rho$, $\varepsilon$, CWP, $C_z$ and $C_e$ all show functionally continuous changes as $\tau$ increases. The rate-change quantities $\rho_{30}$, $\tau_{30}$ and $C_{z30}$ show evidence that they can be monitored until $\tau$ reaches 30, after which their tendencies become more erratic and randomly varying with increasing $\tau$. $\varepsilon_{30}$ and CWP$_{30}$ lose sensitivity to increasing $\tau$, especially when it exceeds 20. For the CI and LI IR indicators, when $\tau \leq 10$, all show values approaching thresholds documented for clear-sky conditions, with the exception being the $\rho$ and $\rho_{30}$ fields (which remain too high). When $11 \leq \tau \leq 20$, $T_B$, $T_{B30}$ and the three IR channel differences 3.9–10.7 μm, 6.5–10.7 μm and 13.3–10.7 μm, all remain in documented clear-sky critical threshold ranges. Once $\tau$ increases beyond 21, only averaged $T_B$ and $T_{B30}$ remain within pre-defined thresholds, yet they possess high contributions from a thick cirrus cloud overcast (i.e. the colder/higher non-cumulus cloud $T_B$'s begin to dominate a scene).

4. The derived GOES VISST parameters that show useful bin-to-bin changes, when the CI and LI interest fields are no longer valuable (specifically when $\tau$ is between 21 and 30), are limited to $\rho_{30}$, $\tau_{30}$, $CWP_{30}$ and $C_{z30}$, given the more linear changes as $\tau$ increases. Specifically, the $\tau_{30}$, $CWP_{30}$ and $C_{z30}$ fields show useful bin-to-bin trends consistent with those expected for deepening cumulus clouds (i.e. increasing $\tau$ and CWP as cloud tops increase in altitude). Since $\rho_{30}$ values fall outside those examined by Harris et al. (2010), namely being positive, more study is required in order to interpret this field with respect to growing convective clouds and LI, albeit the negative trend in $\rho_{30}$ as average $\tau$ increases from 1 to 40 is consistent, providing useful information.

The outcome of this study is that 0–1 h CI and LI nowcasting when cirrus clouds are present is quite feasible, assuming that cloud-derived parameters can be available in a real time fashion (5–15 min after an image is collected), and that a geostationary satellite-based thunderstorm initiation nowcasting algorithm can be designed to identify thin cirrus. The presumption is that as the resolutions (spectral and spatial) of operational geostationary satellite sensors improve, there would be added capability brought by more accurate quantification of cirrus clouds (using channels near ~1.35 μm wavelength, e.g., as expected on GOES-R and the Meteosat Third Generation satellites). Use of more sophisticated statistical and artificial intelligence methods to infer new storm formation from IR and cloud parameter datasets, beyond simple thresholds (e.g., Williams et al., 2008), will help toward more thoroughly exploiting these satellite data for this specific application. All of this innovation will lead to additional advanced lead times for the occurrence of potentially dangerous and severe weather brought by convective storms.

## Acknowledgments

## References

Ackerman, S.A., 1996. Global satellite observations of negative brightness temperature differences between 11 and 6.7 μm. J. Atmos. Sci. 53, 2803–2812.

Berendes, T.A., Mecikalski, J.R., Mackenzie, W.M., Bedka, K.M., Nair, U.S., 2008. Convective cloud detection in satellite imagery using standard deviation limited adaptive clustering. J. Geophys. Res. 113, 20207. http://dx.doi.org/10.1029/2008JD010287.

Browning, K.A., Atlas, D., 1965. Initiation of precipitation in vigorous convective clouds. J. Atmos. Sci. 22, 678–683.

Ellrod, G.P., 2004. Loss of the 12 μm 'split window' band on GOES-M: impacts on volcanic ash detection. J. Volc. Geothermal Res., **135**/1–2. Elsevier, Inc., pp. 91–103.

Haag, W., Kärcher, B., 2004. The impact of aerosols and gravity waves on cirrus clouds at midlatitudes. J. Geophys. Res. 109, D12202. http://dx.doi.org/10.1029/2004JD004579.

Harris, R.J., Mecikalski, J.R., MacKenzie Jr., W.M., Durkee, P.A., Nielsen, K.E., 2010. The definition of GOES infrared lightning initiation interest fields. J. Appl. Meteorol. Climatol. 49, 2527–2543.

Hong, G., Yang, P., Gao, B.-C., Baum, B.A., Hu, Y.X., King, M.D., Platnick, S., 2007. High cloud properties from three years of MODIS Terra and Aqua Collection-4 data over the tropics. J. Appl. Meteorol. Climatol. 46, 1840–1856.

Iskenderian, H., Wolfson, M.M., Ivaldi, C.F., Mecikalski, J.R., MacKenzie Jr., W.M., Feltz, W.F., Bedka, K.M., 2009. Using satellite data to improve convective forecasts in the Collaborative Storm Prediction for Aviation (CoSPA). Proc. First Atmospheric and Space Environments Conf. American Institute of Aeronautics and Astrophysics, San Antonio, TX.

Marshall, J.S., Radhakant, S., 1978. Radar precipitation maps as lightning indicators. J. Appl. Meteorol. 17, 206–212.

Mecikalski, J.R., Bedka, K.M., 2006. Forecasting convective initiation by monitoring the evolution of moving cumulus in daytime GOES imagery. Mon. Wea. Rev. 134, 49–78.

Mecikalski, J.R., Murray, J.J., Feltz, W.F., Johnson, D.B., Bedka, K.M., Bedka, S.T., Wimmers, A.J., Pavolonis, M., Berendes, T.A., Haggerty, J., Minnis, P., Bernstein, B., Williams, E., 2007. Aviation applications for satellite–based observations of cloud properties, convective initiation, in-flight icing, turbulence and volcanic ash. Bull. Am. Meteorol. Soc. 88, 1589–1607.

Mecikalski, J.R., Bedka, K.M., Paech, S.J., Litten, L.A., 2008. A statistical evaluation of GOES cloud-top properties for predicting convective initiation. Mon. Wea. Rev. 136, 4899–4914.

Mecikalski, J.R., MacKenzie, W.M., König, M., Muller, S., 2010. Cloud-top properties of growing cumulus prior to convective initiation as measured by Meteosat Second Generation. Part 1. Use of visible reflectance. J. Appl. Meteorol. Climatol. 49, 2544–2558.

Mecikalski, J.R., Watts, P.D., König, M., 2011. Use of Meteosat Second Generation Optimal Cloud Analysis fields for understanding physical attributes of growing cumulus clouds. Atmos. Res. 102, 175–190.

Min, Q., Duan, M., 2005. Simultaneously retrieving cloud optical depth and effective radius for optically thin clouds. J. Geophys. Res. 110, D21201. http://dx.doi.org/10.1029/2005JD006136.

Min, Q.-L., Harrison, L.C., 1996. Cloud properties derived from surface MFRSR measurements and comparison with GOES results at the ARM SGP site. Geophys. Res. Lett. 23, 1641–1644.

Minnis, P., Nguyen, L., Doelling, D.R., Young, D.F., Miller, W.F., Kratz, D.P., 2002. Rapid calibration of operational and research meteorological satellite imagers, part I: evaluation of research satellite visible channels as references. J. Atmos. Oceanic Technol. 19, 1233–1249.

Minnis, P., Huang, J., Lin, B., Yi, Y., Arduini, R.F., Fan, T.-F., Ayers, J.K., Mace, G.G., 2007. Ice cloud properties in ice-over-water cloud systems using TRMM VIRS and TMI data. J. Geophys. Res. 112, D06206. http://dx.doi.org/10.1029/2006JD007626.

Minnis, P., Nguyen, L., Palikonda, R., Heck, P.W., Spangenberg, D.A., Doelling, D.R., Ayers, J.K., Smith Jr., W.L., Khaiyer, M.M., Trepte, Q.Z., Avey, L.A., Chang, F.-L., Yost, C.R., Chee, T.L., Sun-Mack, S., 2008. Near-real time cloud retrievals from operational and research meteorological satellites. Proc. SPIE Europe Remote Sens. 2008, Cardiff, Wales, UK, 15–18 September, 7107-2. 8 pp.

Minnis, P., Sun-Mack, S., Young, D.F., Heck, P.W., Garber, D.P., Chen, Y., Spangenberg, D.A., Arduini, R.F., Trepte, Q.Z., Smith Jr., W.L., Ayers, J.K., Gibson, S.C., Miller, W.F., Chakrapani, V., Takano, Y., Liou, K.-N., Xie, Y., Yang, P., 2011a. CERES edition-2 cloud property retrievals using TRMM VIRS and Terra and Aqua MODIS data, part I: algorithms. IEEE Trans. Geosci. Remote Sens. 49 (11), 4374–4400.

Minnis, P., Sun-Mack, S., Chen, Y., Khaiyer, M.M., Yi, Y., Ayers, J.K., Brown, R.R., Dong, X., Gibson, S.C., Heck, P.W., Lin, B., Nordeen, M.L., Nguyen, L., Palikonda, R., Smith Jr., W.L., Spangenberg, D.A., Trepte, Q.Z., Xi, B., 2011b. CERES edition-2 cloud property retrievals using TRMM VIRS and Terra and Aqua MODIS data, part II: examples of average results and comparisons with other data. IEEE Trans. Geosci. Remote Sens. 49 (11), 4401–4430.

Mueller, C., Saxen, T., Roberts, R., Wilson, J., Betancourt, T., Dettling, S., Oien, N., Yee, J., 2003. NCAR auto-nowcast system. Wea. Forecasting 18, 545–561.

Murray, J.J., 2002. Aviation weather applications of Earth Science Enterprise data. Earth Observ. Mag. 11 (8), 26–30.

Painemal, D., Minnis, P., Ayers, J.K., OÕNeill, L., in press. GOES-10 microphysical retrievals in marine warm clouds: Multi-instrument validation and daytime cycle over the Southeast Pacific. J. Geophys. Res 117. http://dx.doi.org/10.1029/2012JD017822.

Roberts, R.D., Rutledge, S., 2003. Nowcasting storm initiation and growth using GOES-8 and WSR-88D data. Wea. Forecasting 18, 562–584.

Schmetz, J., Tjemkes, S.A., Gube, M., van de Berg, L., 1997. Monitoring deep convection and convective overshooting with METEOSAT. Adv. Space Res. 19, 433–441.

Schreiber, W.E., 1986. Case study of thunderstorms initiated by radar-observed convergence lines. Mon. Wea. Rev. 114, 2256–2266.

Sieglaff, J.M., Cronce, L.M., Feltz, W.F., Bedka, K.M., Pavolonis, M.J., Heidinger, A.K., 2011. Nowcasting convective storm initiation using satellite-based box-averaged cloud-top cooling and cloud-type trends. J. Appl. Meteorol. Climatol. 50, 110–126.

Smith, W.L., Minnis, P., Finney, H., Palikonda, R., Khaiyer, M.M., 2008. An evaluation of operational GOES-derived single-layer cloud top heights with ARSCL over the ARM Southern Great Plains site. Geophys. Res. Lett. 35, L13820. http://dx.doi.org/10.1029/2008GL034275.

Trishchenko, A.P., Li, Z., Chang, F., Barker, H., 2001. Cloud optical depths and TOA fluxes: comparison between satellite and surface retrievals from multiple platforms. Geophys. Res. Lett. 28 (6), 979–982. http://dx.doi.org/10.1029/2000GL012067.

Walker, J.R., MacKenzie, W.M., Mecikalski, J.R., in press. An enhanced geostationary satellite–based convective initiation algorithm for 0–2 hour nowcasting with object tracking. J. Appl. Meteorol. Climatol.

Watts, P.D., Mutlow, C.T., Baran, A.J., Zavody, A.M., 1998. Study on cloud properties derived from Meteosat second generation observations. EUMETSAT ITT no. 97/181. Final Report. 344 pp. [Available from EUMETSAT, Am Kavalleriesand 31, D–64295 Darmstadt, Germany.].

Westbrook, C.D., Hogan, R.J., Illingworth, A.J., O'Connor, E.J., 2007. Theory and observations of ice particle evolution in cirrus using Doppler radar: evidence for aggregation. Geophys. Res. Lett. 34, L02824. http://dx.doi.org/10.1029/2006GL027863.

Wielicki, B.A., Barkstrom, B.R., Baum, B.A., Charlock, T.P., Green, R.N., Kratz, D.P., Lee, R.B., Minnis, P., Smith, G.L., Wong, T., Young, D.F., Cess, R.D., Coakley, J.A., Crommelynck, D.A.H., Donner, L., Kandel, R., King, M.D., Miller, A.J., Ramanathan, V., Randall, D.A., Stowe, L.L., Welch, R.M., 1998. Clouds and the Earth's Radiant Energy System (CERES): algorithm overview. IEEE Trans. Geosci. Remote Sens. 36 (4), 1127–1141.

Williams, J.K., Ahijevych, D., Dettling, S., Steiner, M., 2008. Combining observations and model data for short-term storm forecasting. Proc. SPIE 7088, 708805. http://dx.doi.org/10.1117/12.795737.

Wilson, J.W., Mueller, C.K., 1993. Nowcasts of thunderstorm initiation and evolution. Wea. Forecasting 8, 113–131.

Wilson, J.W., Schriber, W.E., 1986. Initiation of convective storms by radar-observed boundary layer convergent lines. Mon. Wea. Rev. 114, 2516–2536.

Wilson, J.W., Foote, G.B., Crook, N.A., Fankhauser, J.C., Wade, C.G., Tuttle, J.D., Mueller, C.K., Kruger, S.K., 1992. The role of boundary-layer convergence zones and horizontal rolls in the initiation of thunderstorms. A case study. Mon. Wea. Rev. 120, 1785–1815.

Zhang, J., Howard, K., Langston, C., Vasiloff, S., Kaney, B., Arthur, A., Cooten, S.V., Kelleher, K., Kitzmiller, D., Ding, F., Seo, D.-J., Wells, E., Dempsey, C., 2011. National Mosaic and Multi-sensor QPE (NMQ) system—description, results and future plans. Bull. Am. Meteorol. Soc. 92, 1321–1338.

Zheng, X., Albrecht, B., Jonson, H., Khelif, D., Feingold, G., Minnis, P., Ayers, K., Donaher, S., Rossiter, D., Ruiz-Plancarte, J., Sun-Mack, S., 2011. Observations of the boundary layer, cloud, and aerosol variability in the southeast Pacific coastal marine stratocumulus during VOCALS-Rex. Atmos. Chem. Phys. 11, 9943–9959.